



# Binding Fe-doped g-C<sub>3</sub>N<sub>4</sub> on the porous diatomite for efficient degradation of tetracycline via photo-Fenton process

Yu Zhang<sup>a</sup>, Xing Chen<sup>a,b,\*</sup>, Min-Shu Cui<sup>b</sup>, Zhi Guo<sup>b</sup>, Yi-Han Chen<sup>b</sup>, Kang-Ping Cui<sup>b</sup>, Zhao-Gang Ding<sup>b</sup>, Rohan Weerasooriya<sup>a,c</sup>

<sup>a</sup> Key Lab of Aerospace Structural Parts Forming Technology and Equipment of Anhui Province, Institute of Industry and Equipment Technology, Hefei University of Technology, Hefei 230009, PR China

<sup>b</sup> Key Laboratory of Nanominerals and Pollution Control of Higher Education Institutes, School of Resources and Environmental Engineering, Hefei University of Technology, Hefei 230009, PR China

<sup>c</sup> National Centre for Water Quality Research, National Institute of Fundamental Studies, Hantana, Kandy, Sri Lanka

## ARTICLE INFO

Editor: Dr. Zhang Xiwang

### Keywords:

Fe-doped g-C<sub>3</sub>N<sub>4</sub>

Diatomite

Photo-Fenton process

Tetracyclines

## ABSTRACT

We fabricated iron-doped carbon nitride on a diatomite surface through a single-step polymerization (FGD-x, where x represents Fe loading content). The FGD-x efficiently degrades tetracycline hydrochloride by a collaborative photo-Fenton process. The FGD-3 (FeCl<sub>3</sub> loading 75 mg) showed the best catalytic performance in TC degradation with minimal H<sub>2</sub>O<sub>2</sub> (viz. 1 mmol/L) at a wide pH range (2.0–7.0). Under optimized conditions, the FGD-3 can degrade 98.3% of 20.0 mg/L TC at pH 4.0 within 100 min under visible light irradiation. The scanning electron microscopic and X-ray photon spectroscopic data show that iron is successfully doped on g-C<sub>3</sub>N<sub>4</sub>. Electrochemical impedance spectroscopy and transient photocurrent performance analyses confirmed that photogenerated electrons rapidly transfer at FGD-3 and solution interface. Free radical quenching experiments and electron spin resonance analysis show that h<sup>+</sup>, •O<sub>2</sub><sup>-</sup>, and •OH can degrade TC efficiently. Besides, FGD-3 has an ultra-high catalytic activity and extremely low iron leaching after repeated use. The FGD-3 provides a feasible way to design a new photo-Fenton catalyst for the destruction of organic pollutants from water.

## 1. Introduction

Tetracycline is a widely used antibiotic in human and veterinary medical applications. However, tetracycline is weakly absorbed in the body, which results in its direct discharge into the environment, causing serious problems to ecosystem health [1–3]. Tetracycline remediation methods in water include adsorption [4], membrane separation [5], chemical oxidation [6], photocatalysis [7], and biological degradation [8]. The treatment methods based on adsorption or membrane separation merely concentrate the pollutant into another compartment/phase without really destroying it [9]. The chemical or photocatalysis mediated tetracycline degradation results in intermediates that require special attention.

On the other hand, biological treatment methods' efficiency diminishes over time due to tetracycline's antibiotic properties or its by-products. Photo-Fenton technology effectively destructs refractory organic pollutants as tetracycline. The catalyst used in these methods

can recycle and be economical [10]. Photo-Fenton technology overcomes problems such as low efficiency and stringent solution acidity requirements associated with homogeneous Fenton reaction. However, photo-Fenton and Fenton processes are prone to generate iron slag and other shortcomings [11]. As a novel semiconductor photocatalyst, g-C<sub>3</sub>N<sub>4</sub> has attracted much attention due to its good chemical stability and visible light response [12]. However, its low specific surface area, fast recombination of photogenerated electron and hole pair, and narrow visible light absorption range restrict g-C<sub>3</sub>N<sub>4</sub>'s catalytic activity [13, 14]. At present, many strategies applied to prevent e<sup>-</sup> and h<sup>+</sup> recombination of g-C<sub>3</sub>N<sub>4</sub> have been found. These strategies include substrate's structural modifications [15], metallic or nonmetallic doping [16, 17], precious metal deposition [18], and construction of heterojunctions [19]. A semiconductor bandgap is vital for efficient charge transfer by doping with metal ions [20]. Zhang et al. [21] prepared a Co/g-C<sub>3</sub>N<sub>4</sub> photocatalyst. Co's doping causes the absorption spectrum of the Co/g-C<sub>3</sub>N<sub>4</sub> to redshift, and the recombination rate of the photogenerated

\* Corresponding author at: Key Lab of Aerospace Structural Parts Forming Technology and Equipment of Anhui Province, Institute of Industry and Equipment Technology, Hefei University of Technology, Hefei 230009, PR China.

E-mail address: [xingchen@hfut.edu.cn](mailto:xingchen@hfut.edu.cn) (X. Chen).

<https://doi.org/10.1016/j.jece.2022.107406>

Received 24 November 2021; Received in revised form 6 January 2022; Accepted 12 February 2022

Available online 16 February 2022

2213-3437/© 2022 Elsevier Ltd. All rights reserved.

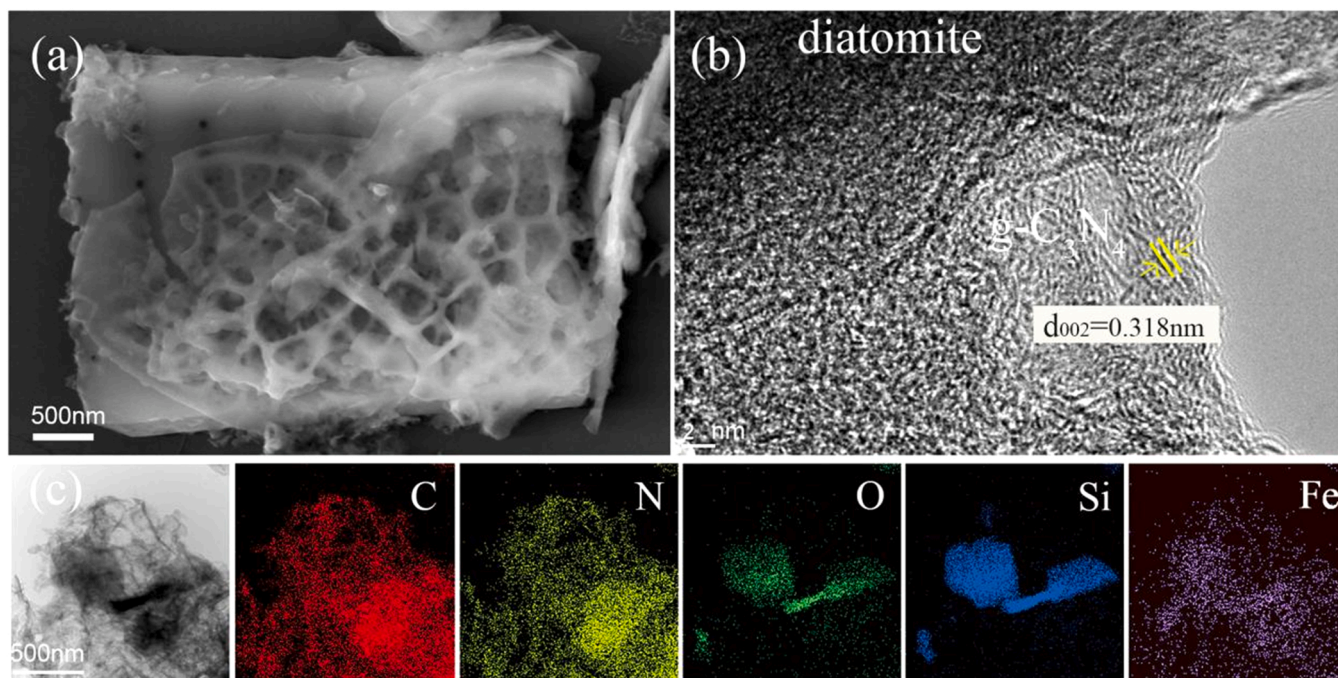


Fig. 1. SEM (a) and HRTEM images (b), and elemental mapping images (c) of FGD-3.

electron-hole pair is reduced. The catalyst's visible light absorption efficiency has increased, showing its excellent performance for methylene blue degradation. Wang et al. [22] prepared porous Fe-g-C<sub>3</sub>N<sub>4</sub> nanosheets with different Fe loading. The bonding between pyridine N and Fe atoms in g-C<sub>3</sub>N<sub>4</sub> enhances the electron transport rate, limits iron ions leaching thus curtailing secondary environmental pollution. However, g-C<sub>3</sub>N<sub>4</sub> is easy to agglomerate by thermal polymerization, which greatly reduces the catalytic activity. The agglomeration problem can be solved by fixing g-C<sub>3</sub>N<sub>4</sub> nanosheets on porous substrates or templates [23,24]. As a natural mineral material, diatomite has a stable porous structure with a large specific surface area. And also, there are a large number of silicon hydroxyl groups and hydrogen bonds on the surface, which makes the diatomite's strong adsorption ability [25,26]. The performance of the photocatalyst to remediate recalcitrant pollutants can be improved by fixing it on the surface of diatomite or allied substrate in constructing a composite material with multi-elements [27].

Presently, we fabricated a well-dispersed, iron-doped g-C<sub>3</sub>N<sub>4</sub> composite (FGD-x, where x represents Fe loading content) using urea and FeCl<sub>3</sub> on a diatomite surface to be suited for efficient reactivity under visible light irradiation (Fig. S1). As a heterogeneous catalyst, the new composite operates via two modes, viz. photocatalysis and the Fenton process. Tetracycline was used as a probe to assess the catalytic reactivity of the composite. The mechanism of TC degradation by the photo-Fenton process was examined with LC-MS, free radical capture experiments, and electron spin resonance spectroscopy methods. In addition, the stability of the catalyst was studied through repeated experiments.

## 2. Experiments

### 2.1. Materials and chemicals

Diatomite was purchased from International Building Materials Environmental Technology Co., Ltd. Urea, anhydrous iron trichloride (FeCl<sub>3</sub>), purchased from Sinopharm Chemical Reagent Co., Ltd, China. Hydrochloric acid (HCl), sodium hydroxide (NaOH), hydrogen peroxide (H<sub>2</sub>O<sub>2</sub>), tetracycline hydrochloride (TC·HCl), sodium sulfate (Na<sub>2</sub>SO<sub>4</sub>), tert-butanol (TBA), disodium ethylenediaminetetraacetic acid (EDTA-2Na), and 1,4-benzoquinone (BQ) were all purchased from Shanghai

Maclean's Chemical Co., Ltd., China. All experiments use deionized water, and all the chemical reagents used in the experiment are of analytical grade.

### 2.2. Synthesis of Fe-g-C<sub>3</sub>N<sub>4</sub>/DE

The Fe-g-C<sub>3</sub>N<sub>4</sub>/DE composite material is prepared and synthesized by a single-step thermal polymerization method. First, 10.0 g urea and 1.0 g diatomite were dispersed in 50 mL deionized water while adding pre-determined aliquots of FeCl<sub>3</sub>, and the mixture was ultrasonicated for 30 min. Evenly dispersed diatomite mixture was then slowly added to the above solution maintained at 60 °C and stirred to evaporate the water. The resulting composite was dried in a tube furnace at 550 °C (heating rate 5 °C/min) for 2 h under continuous nitrogen (99.999%) purging. The FeCl<sub>3</sub> content added in the composite was varied from 25 to 100 mg at 25 mg intervals, and the resultant substrates were designated as FGD-1, FGD-2, FGD-3, and FGD-4, respectively. The preparation methods of pure g-C<sub>3</sub>N<sub>4</sub>, Fe/DE(FD), and g-C<sub>3</sub>N<sub>4</sub>/DE(GD) are in the Supporting InformationText S1.

### 2.3. Catalyst characterization

The morphology, microstructure, and element composition of the prepared samples were studied using SU-8020 thermal field emission scanning electron microscope (SEM, Hitachi, Tokyo), JEM-2100F transmission electron microscopy (HRTEM, JEOL, Japan), and energy-dispersive X-ray spectrometer (EDS). The phase structures of the prepared samples in the range of  $2\theta = 10^\circ - 70^\circ$  were studied using an X-Pert PRO MPD fixed-target X-ray diffractometer (XRD, PANalytical, Netherlands). The chemical properties of the samples were studied by Fourier infrared spectrometer (FT-IR, Thermo Nicolet, USA). The surface chemical properties of the samples were studied by an X-ray photoelectron spectrometer (XPS, Thermo, USA), and the C1s, O1s, N1s, Si2p, and Fe2p spectra of the samples were analyzed by advantage software. The specific surface area and the pore size distribution of the samples were determined by Brunauer-Emmett-Teller analyzer (Autosorb-IQ3, Quantachrome, USA). UV-vis-NIR diffuse reflectance spectra (DRS) of the samples were obtained against the BaSO<sub>4</sub> reference (Cary 5000,

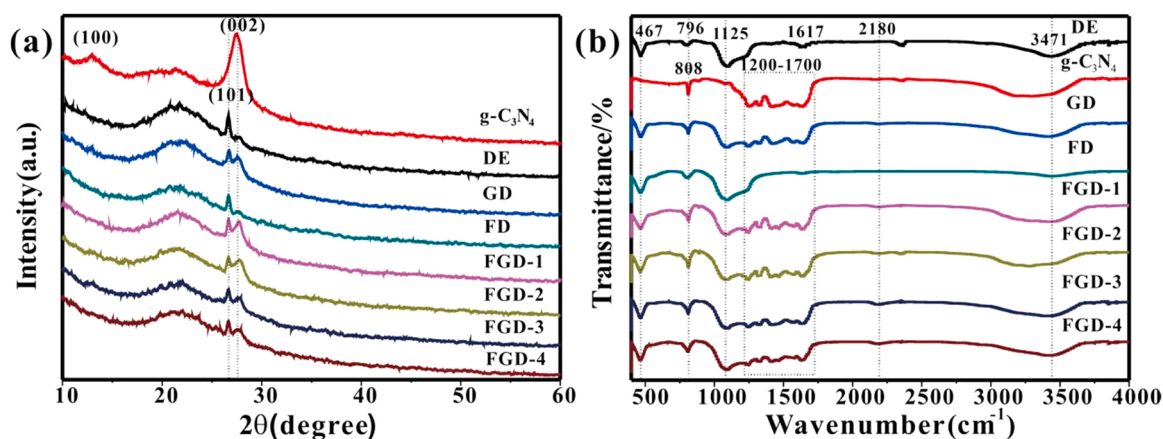


Fig. 2. The XRD patterns (a) and FT-IR spectra (b) of synthesized photocatalysts.

USA).

#### 2.4. Photo-Fenton catalytic activity

The photocatalytic performance of the prepared samples was evaluated by degradation of TC solution under the irradiation of a 500 W xenon lamp. In the degradation experiment, 10 mg of catalyst was added to 25 mL of TC aqueous solution at an initial concentration of 20 mg/L. After adding the solution, the sample reacted in darkness for 30 min to reach the equilibrium of adsorption-desorption. Irradiation before joining a certain concentration of  $H_2O_2$ , 20 min intervals in a certain volume of the reaction solution, and use a 0.45  $\mu m$  filter membrane to

filter to remove the catalyst.

#### 2.5. Analysis methods

The TC concentration was investigated by liquid chromatography (LC, Shimadzu LC-20A, Japan) equipped with an SPD-20A UV-Vis detector and C18 column ( $4.6 \times 250$  mm). The detection wavelength was 355 nm. The mobile phase was using 20% acetonitrile and 80% 10 mM oxalic acid solution at a flow rate of 1.0 mL/min. The degraded intermediate was analyzed by high-performance liquid chromatography-mass spectrometry (HPLC-MS, Agilent 1290/6460, USA). The degree of mineralization of TC was evaluated by TOC/TN analysis (Multi-N/

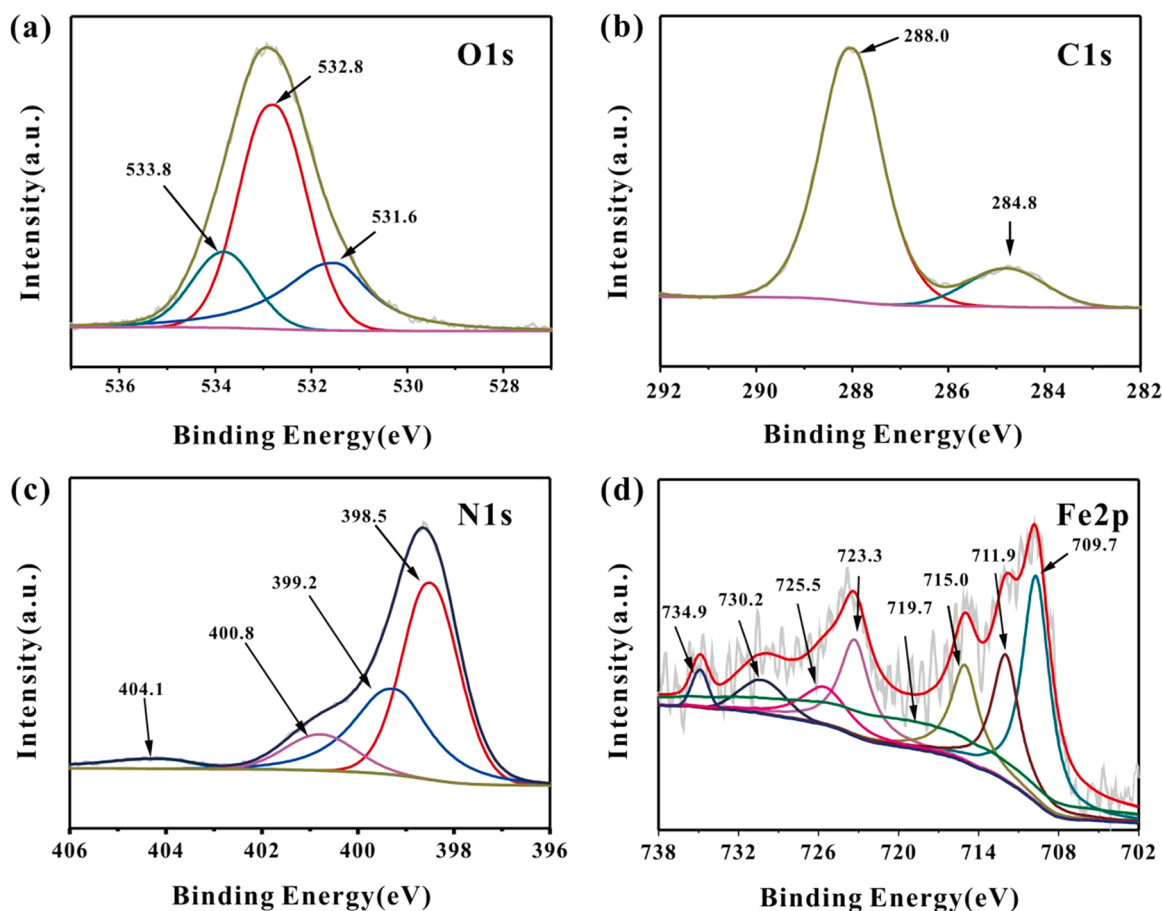


Fig. 3. XPS spectra of O1s(a), C1s (b), N1s (c) and Fe2p (d) for FGD-3.

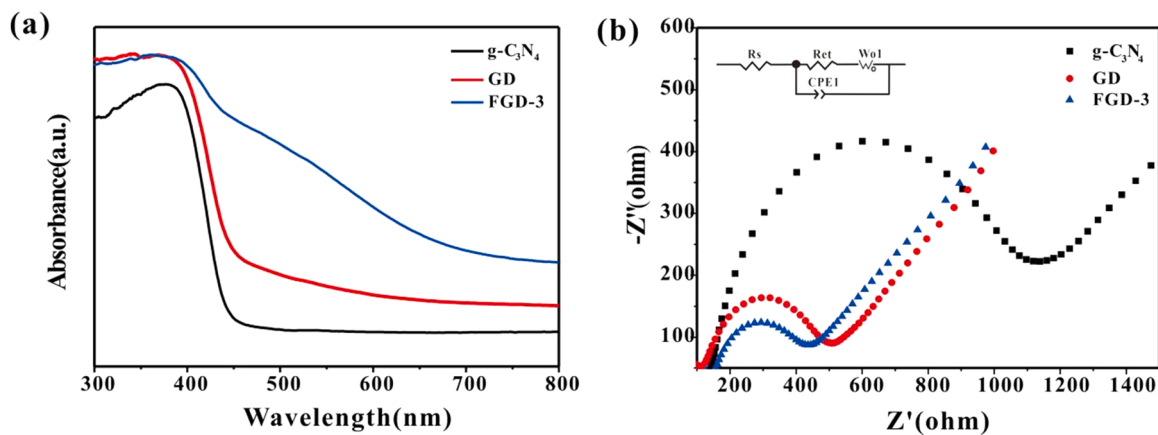


Fig. 4. UV-DRS spectra (a) and EIS Nyquist plots (b) of as-prepared catalysts.

c3100). The electron paramagnetic resonance spectroscopic method (ESR, Bruker, Germany) was used to detect  $\cdot\text{OH}$  and  $\cdot\text{O}_2^-$  radicals, using DMPO as scavengers.

### 3. Results and discussion

#### 3.1. Structural and morphological characterizations

The SEM morphology of diatomite,  $\text{g-C}_3\text{N}_4$ , GD, and FGD-3 composites are shown in Fig. S2. and Fig. 1. Diatomite has a disc-shaped, porous structure with a diameter of 30  $\mu\text{m}$ ; many broken diatom cells are also observed, which are ideal for hosting the catalyst (Fig. S2a). The  $\text{g-C}_3\text{N}_4$  has a layered structure with irregular surface morphology and agglomeration (Fig. S2b). Fig. S2c shows the microstructure of GD, where  $\text{g-C}_3\text{N}_4$  is loaded on the diatomite surface. However, the GD morphology did not change even after Fe doping (Fig. 1a). Compared to  $\text{g-C}_3\text{N}_4$ , when loaded to diatomite, the distribution of  $\text{g-C}_3\text{N}_4$  is even: this arrangement resolved the agglomeration problem of  $\text{g-C}_3\text{N}_4$  particulates; the diatomite enhanced the contact area between the catalyst and the pollutant; it also facilitated photogenerated carriers' migration by improving quantum efficiency [27]. Fig. 1b is the HRTEM image of FGD-3. The crystal planes of  $\text{g-C}_3\text{N}_4$  (002) and the lattice fringes with a spacing of 0.318 nm can be found. EDS data (Fig. 1c) show that the prepared FGD-3 composite is mainly composed of C, N, O, Si and Fe, and the elements of C, N, and Fe are evenly distributed on the surface of diatomite, which further confirms the existence of Fe doping on FGD-3.

Fig. 2a shows the X-ray diffractograms of all samples used for TC removal/ degradation. The crystal structure of the  $\text{g-C}_3\text{N}_4$  shows two peaks around  $13.2^\circ$  and  $27.6^\circ$  corresponding to (100) and (002) crystal planes (JCPDS No. 87-1526). The broad hump shown in the X-ray diffractogram characterizes the amorphous nature of diatomite. The peak at  $26.6^\circ$  corresponds to the  $\text{SiO}_2$  (101) crystal plane (JCPDS No. 46-1045). The diffraction pattern of GD sample shows two main peaks at  $26.6^\circ$  and  $27.6^\circ$ , corresponding to  $\text{SiO}_2$  (101) crystal plane and  $\text{g-C}_3\text{N}_4$  (002) crystal plane respectively. After Fe doping, the peak corresponding to (100) crystal plane disappeared and the intensity of the peak corresponding to (002) crystal plane of  $\text{g-C}_3\text{N}_4$  decreased gradually with the increase of Fe doping amount, indicating the Fe doping destroyed the intrinsic periodic structure of  $\text{g-C}_3\text{N}_4$  by the coordination  $\text{Fe-N}_x$  bond [28].

To determine the nature of functional groups on the new composites, we used FTIR and XPS measurements data. As shown in Fig. 2b, strong IR peaks are observed in diatomite at  $3471\text{ cm}^{-1}$ ,  $1617\text{ cm}^{-1}$ ,  $1125\text{ cm}^{-1}$ ,  $796\text{ cm}^{-1}$ , and  $467\text{ cm}^{-1}$  (Fig. 2b). The peaks at  $467\text{ cm}^{-1}$  and  $1125\text{ cm}^{-1}$  are due to asymmetric stretching vibrations of Si-O-Si in diatomite [29,30]. The wide peaks at  $3471\text{ cm}^{-1}$  and  $1617\text{ cm}^{-1}$  are due to H-OH stretching and bending vibration of adsorbed water,

respectively [31]. The peak observed at  $796\text{ cm}^{-1}$  is attributed to the Si-O-Al bond bending. The wide IR bands of  $\text{g-C}_3\text{N}_4$  shown between  $3700$  and  $3000\text{ cm}^{-1}$  are derived from the tensile vibrations of N-H and O-H, which indicate the presence of amino and adsorbed hydroxyl species on the nanosheets. The peaks in the range of  $1200\text{--}1700\text{ cm}^{-1}$  are due to tensile vibrations of C-N and C=N of the heterocyclic ring [32]. The peak at  $808\text{ cm}^{-1}$  corresponds to ring vibrations of tri-s-triazine [33]. But there is no significant difference in the FT-IR spectra among Fe-doped composites, diatomite, and  $\text{g-C}_3\text{N}_4$ , indicating that the composite's chemical structure has not changed. However, with the increase of Fe content, CN heterocycles' peak strength weakens, which confirms the successful doping of Fe into  $\text{g-C}_3\text{N}_4$ . A new peak appears at  $2180\text{ cm}^{-1}$  with the increase of Fe content attributed to C-N's tensile vibration [34].

The XPS characterization was performed to identify the chemical state of the composites. Fig. S3a shows the wide-scan XPS spectrum of FGD-3. The peak at  $103.7\text{ eV}$  corresponds to Si-O in diatomite (Fig. S3b). The peaks at  $531.6$ ,  $532.8$ , and  $533.8\text{ eV}$  are due to N-C-O, OH, and Si-O groups, respectively, on diatomite surface (O1s spectrum, Fig. 3a) [27]. This indicates that diatomite acts as a carrier in hosting the composite. The C1s spectrum can be resolved into two peaks at  $284.8$  and  $288.0\text{ eV}$ , which are attributed to C-C [24] and  $\text{sp}^2$  carbon (N-C=N), respectively (Fig. 3b) [35]. The N1s spectrum (Fig. 3c) has resolved into four peaks. The peaks at  $398.5$ ,  $399.2$ , and  $400.8\text{ eV}$  are ascribed to C=N-C, N-(C)<sub>3</sub>, and N-H in the  $\text{g-C}_3\text{N}_4$  network [27,36,37]. Compared with N1s of GD in Fig. S4, the binding energy of FGD-3 ( $398.5\text{ eV}$ ) is higher than the pyridinic N in GD ( $398.3\text{ eV}$ ), which might be due to the formation of the Fe-N bond [38,39]. The peak at  $404.1\text{ eV}$  occurs due to charging effects [40]. Besides, eight peaks are used, fitting the Fe2p spectrum of FGD-3 (Fig. 3d). The peaks at  $709.7\text{ eV}$ ,  $711.9\text{ eV}$ ,  $723.3\text{ eV}$  and  $725.5\text{ eV}$  are assigned to  $\text{Fe}^{2+}2\text{p}_{3/2}$ ,  $\text{Fe}^{3+}2\text{p}_{3/2}$ ,  $\text{Fe}^{2+}2\text{p}_{1/2}$  and  $\text{Fe}^{3+}2\text{p}_{1/2}$ , respectively, which indicate that doped Fe has two chemical states. The other four broad bands are satellite peaks of  $\text{Fe}^{2+}$  and  $\text{Fe}^{3+}$  [41]. The above results confirm the successful synthesis of FGD-3 composites. The XPS analysis of FGD-3 after the reaction was also investigated. The O1s, N1s, C1s, and Fe2p of FGD-3 after the reaction are shown in Fig. S3. It can be found that the XPS spectrum of the catalyst after the reaction had a slightly chemical shift. Through the results of experiments and characterization, we speculate that the changes in XPS spectra before and after the reaction might be attributed to the following factors: (1) The Fe-N bond has been destroyed to a certain extent during the reaction, which results in the leaching of iron and the change of N1s binding energy. (2) TC and its degradation products after the reaction contains C, N and O elements, which would contribute to the change of the energy spectrum of the recovered catalyst for the adsorption effect. (3) The reactive oxygen species (ROS) generated in the catalytic reaction might also damage the heptazine ring of  $\text{g-C}_3\text{N}_4$ , so the energy spectrum

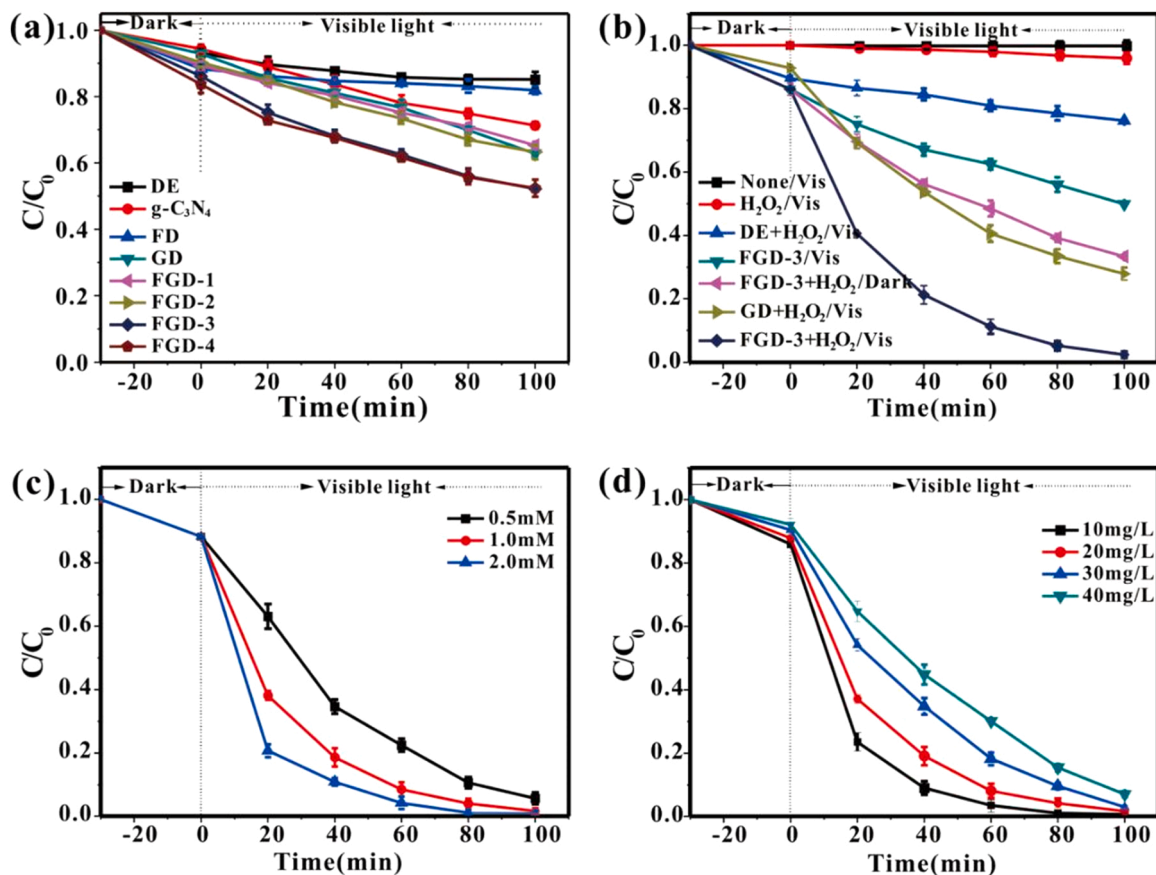


Fig. 5. The effects of various parameters on the TC degradation in FGD-3 catalyzed photo-Fenton system: (a) different catalysts without addition of H<sub>2</sub>O<sub>2</sub> (Reaction conditions: pH 4.0; initial TC, 20.0 mg/L; catalyst, 400 mg/L.); (b) different reaction systems (Reaction conditions: pH 4.0; initial TC, 20.0 mg/L; catalyst, 400 mg/L; H<sub>2</sub>O<sub>2</sub>, 1.0 mM); (c) H<sub>2</sub>O<sub>2</sub> concentration (Reaction conditions: pH 4.0; initial TC, 20.0 mg/L; catalyst, 400 mg/L) (D) initial TC concentration (Reaction conditions: pH 4.0; catalyst, 400 mg/L; H<sub>2</sub>O<sub>2</sub>, 1.0 mM).

of C1s and N1s after the reaction change slightly [42].

Diatomite is used as an ideal carrier for supporting photocatalysts due to its unique porous structure. The raw diatomite and the composite materials were characterized by BET as shown in Fig. S5a. The nitrogen adsorption and desorption curves of the three materials followed typical II curves, showing the microporous and macroporous structures for the adsorption of pollutants. The specific surface area of the raw diatomite is 37.127 m<sup>2</sup>/g, and the pore size distribution is around 59.849 nm. After loading the photocatalyst, the specific surface area of the catalyst decreases. As mentioned before, there are many macroporous and microporous structures on the surface of diatomite. When g-C<sub>3</sub>N<sub>4</sub> was loaded, the microporous structures were partially covered with stacked g-C<sub>3</sub>N<sub>4</sub>, and most of the macroporous structures remained, so the specific surface area decreased. For FGD-3, the Fe doping might change the structure of g-C<sub>3</sub>N<sub>4</sub> on the surface of diatomite, generating more porous structures and enlarging its specific surface area [43], which would provide FGD-3 with a larger contact interface and expose more active sites.

The effect of Fe doping on optical properties of FGD-3 was also examined by UV-Vis diffuse reflectance spectroscopy (DRS). As shown in Fig. 4(a), all samples show distinct absorption edges. Compared to g-C<sub>3</sub>N<sub>4</sub> (absorption edge  $\lambda = 420$  nm), both GD and FGD-3 show a redshift. This effect is marked in FGD-3 due to doped Fe in g-C<sub>3</sub>N<sub>4</sub> lattice that results in distorted band structure; Therefore, in FGD-3, the electrons can shuttle easily between conduction and valence bands of perturbed g-C<sub>3</sub>N<sub>4</sub>. Further, the bandgap energy (E<sub>g</sub>) is estimated by a Tauc plot using the Kubelka-Munk function:

$$\alpha hv = A(hv - E_g)^n \quad (1)$$

where  $\alpha$  represents the absorption coefficient,  $h$  is the Planck constant,  $v$  is the optical frequency,  $E_g$  is the bandgap energy,  $A$  is a constant, and  $n$  depends on the characteristics of the semiconductor transition (i.e., direct transition ( $n = 1/2$ ) or indirect transition ( $n = 2$ )) [21,44]. As shown in the data, g-C<sub>3</sub>N<sub>4</sub> shows the indirect transition ( $n = 2$ ). The bandgap energy (E<sub>g</sub>) of FGD-3 as estimated by  $(\alpha hv)^{1/2}$  vs  $hv$  plots is shown in Fig. S5b. The calculated band gaps were reduced from 2.81 eV for pure g-C<sub>3</sub>N<sub>4</sub> to 2.31 eV for FGD-3. The valence band potential of FGD-3 is 1.44 eV, which is higher than the theoretical value of pure g-C<sub>3</sub>N<sub>4</sub> of 1.40 eV (Fig. S5c). Therefore, the conduction band potential is estimated at -0.87 eV. Thus the electrons generated can reduce  $Fe^{3+} \rightarrow Fe^{2+}$  ( $E^0(Fe^{3+}/Fe^{2+}) = 0.771$  eV to NHE), which favors cycling of iron species in Photo-Fenton reaction [45].

The charge transfer efficiency between FGD-3, g-C<sub>3</sub>N<sub>4</sub>, or GD and solution interface was determined by electrochemical impedance spectroscopy (EIS), as shown in Fig. 4b. The Nyquist radius of EIS spectrums measures charges transfer resistance in the interfacial region. The electrochemical impedance data of the modified electrode were further analyzed via the equivalent circuit simulation (inset of Fig. 4b). Table S1 shows the circuit simulation parameters, and the resistances of g-C<sub>3</sub>N<sub>4</sub>, GD, and FGD-3 are 922.8  $\Omega$ , 395.8  $\Omega$ , and 314.1  $\Omega$ , respectively. It can be found that the FGD-3 modified electrode's Nyquist arc radius is the smallest, indicating that the Fe doping in the FGD-3 improves the charge transfer efficiency [46].

The photocurrent responses of pure g-C<sub>3</sub>N<sub>4</sub>, GD, and FGD-3 composites under the illumination of the Xe lamp are shown in Fig S5d. The photocurrent response of the FGD-3 is the highest. This indicates that the doped Fe in the composite has increased the charge transferring capacity of the catalyst. For pure g-C<sub>3</sub>N<sub>4</sub> or GD, electrons' separation efficiency

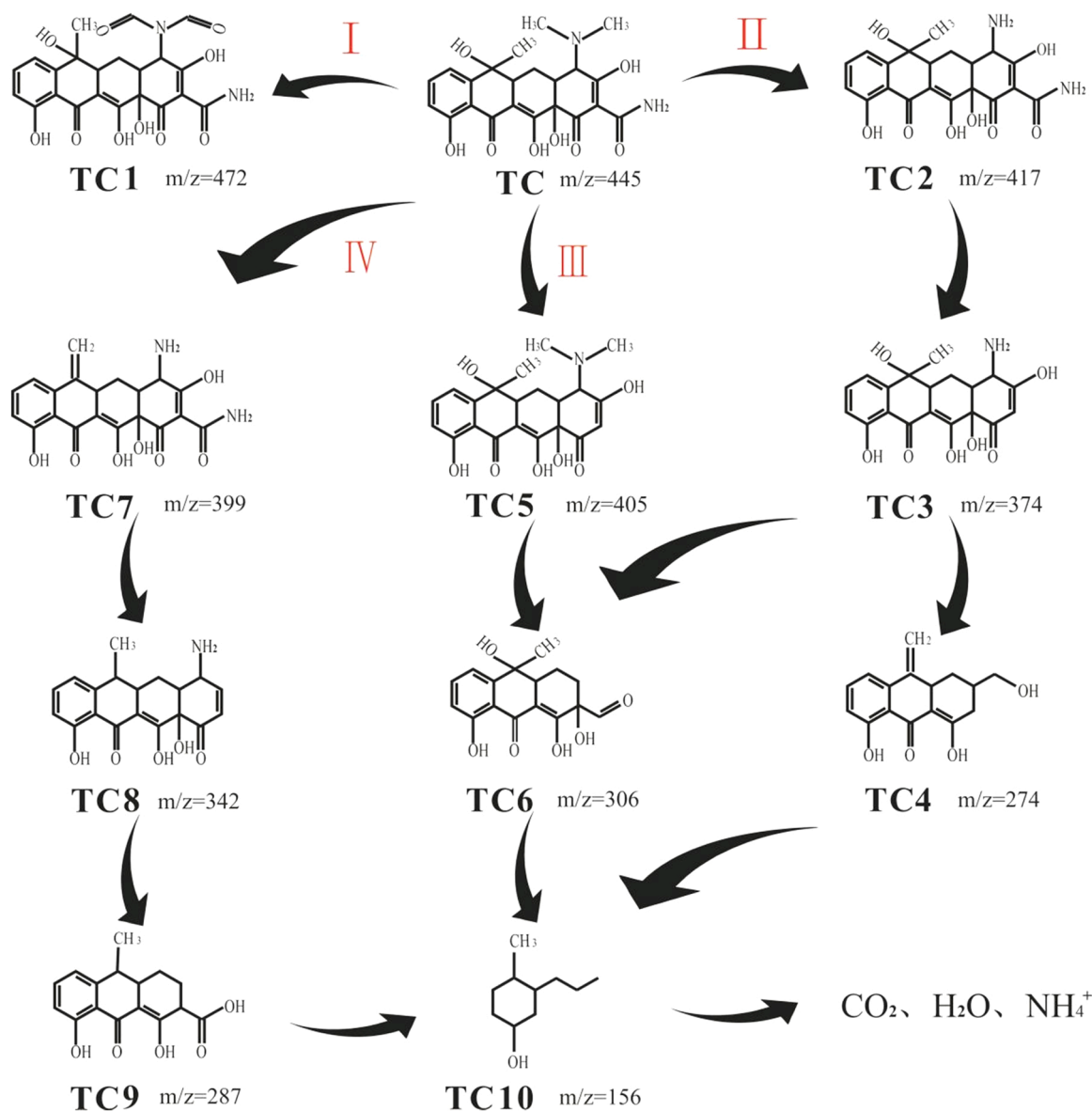


Fig. 6. Proposed degradation pathways of TC in the FGD-3 Photo-Fenton system.

would be suppressed by the recombination of photogenerated electron-hole. Therefore, FGD-3 might have high photo-Fenton catalytic activities [45].

Fig. S6 shows the Raman spectra of pure  $\text{g-C}_3\text{N}_4$ , GD, and FGD-3. The D and G bands at  $1345$  and  $1560\text{ cm}^{-1}$  represent the existence of defects of  $\text{sp}^3$  hybridized carbon atoms and in-plane stretching vibration of carbon atom  $\text{sp}^2$  hybridized, respectively [47]. In addition, the peak at  $752\text{ cm}^{-1}$  is associated with the bending vibrations of melon, and the vibration at  $472\text{ cm}^{-1}$  and  $1228\text{ cm}^{-1}$  belong to heptazine rings in melon/melon units [48]. It can be found that the typical peaks appear in all these three samples, verifying the characterization of  $\text{g-C}_3\text{N}_4$  [49].

### 3.2. Photo-Fenton catalytic activity

The photocatalytic activity of FGD samples with different Fe doping amounts was evaluated by visible light irradiation degradation of TC. Meanwhile, DE,  $\text{g-C}_3\text{N}_4$ , FD, and GD were compared. Before evaluating the photocatalytic properties of the catalysts, the adsorption experiments were performed in the dark (shown in Fig. S7). The adsorption equilibriums of the catalysts were reached in about 30 min, and their removal ratios were no more than 20%. So, all the photocatalytic

experiments were performed after the adsorption for 30 min. The photocatalytic performances of the catalysts under the visible light irradiation for 100 min are shown in Fig. 5a. It can be found that DE and FD have only adsorption effect on TC after 100 min irradiation, and  $\text{g-C}_3\text{N}_4$ , GD and FGD composites with different doping amounts of Fe have photocatalytic degradation effects under visible light irradiation. Among them, FGD-3 and FGD-4 both have high photocatalytic effects, and the degradation effect can reach about 50%, indicating that the appropriate amount of Fe doping can improve the photocatalytic effect of the catalyst. However, FGD-4 has a higher adsorption effect after the dark adsorption reaches the adsorption equilibrium, and FGD-3 has a better photocatalytic effect under visible light irradiation.

Fig. 5b demonstrates the effects of visible light and  $\text{H}_2\text{O}_2$  on the photocatalytic degradation of TC degradation. Under the visible light irradiation, only a very low amount of  $\cdot\text{OH}$  was produced with the addition of  $\text{H}_2\text{O}_2$  and DE, so TC was slightly degraded. However, for GD, after adding  $\text{H}_2\text{O}_2$  under the visible light irradiation, the degradation ratio reached 72%. Interestingly, FGD-3 and  $\text{H}_2\text{O}_2$  have degradation effects under both light and dark conditions. The degradation effect under the dark conditions might be due to the Fenton reaction between Fe and  $\text{H}_2\text{O}_2$  in FGD-3. Under visible light irradiation, FGD-3 and  $\text{H}_2\text{O}_2$

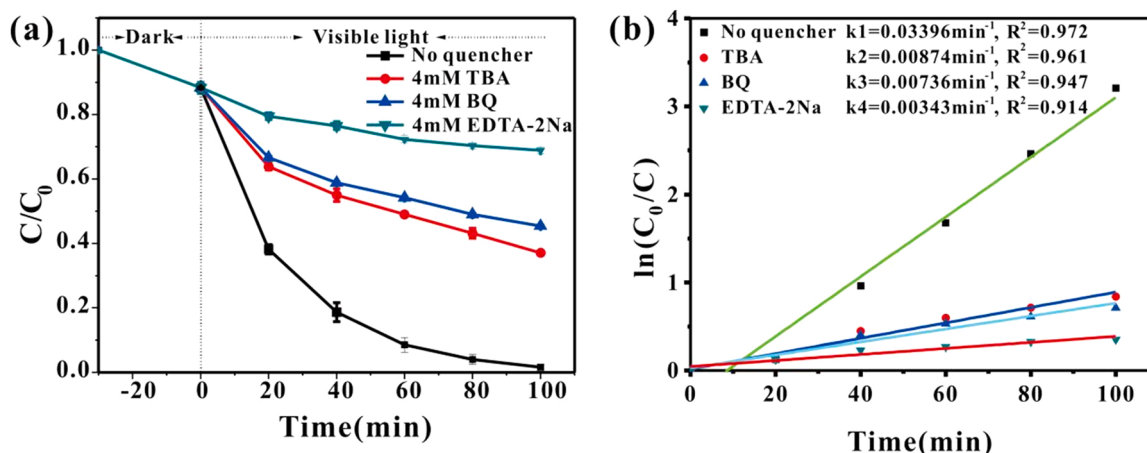


Fig. 7. (a) Effect of radical scavengers on the degradation of TC and (b) rate constants for the degradation of TC with or without various trapping agents. (Reaction conditions: pH 4.0; initial TC, 20.0 mg/L; catalyst, 400 mg/L; H<sub>2</sub>O<sub>2</sub>, 1.0 mM).

produced a synergistic photo-Fenton reaction, and the degradation effect was significantly higher than that of photocatalysis and Fenton catalysis, so the reaction speed was improved. To further demonstrate the role of diatomite in FGD-3, the catalytic activities of Fe-g-C<sub>3</sub>N<sub>4</sub> (FG) and FGD-3 were compared as shown in Fig. S8. Under the visible light irradiation, the synergistic effect of FG/H<sub>2</sub>O<sub>2</sub>/ light is lower than that of FGD-3/H<sub>2</sub>O<sub>2</sub>/ light, indicating that the porous diatomite is one of the most ideal materials for loading catalysts, which can supply more activated sites.

As shown in Fig. 5c, the effect of H<sub>2</sub>O<sub>2</sub> concentration on the degradation effect of TC was studied. It can be seen that as the concentration of H<sub>2</sub>O<sub>2</sub> increases, the degradation effect of FGD-3 on TC increases significantly. When the concentration of H<sub>2</sub>O<sub>2</sub> is 0.5 mmol/L, the reaction rate is relatively slow, the degradation efficiency is about 93%, with the ascension of H<sub>2</sub>O<sub>2</sub> concentration, reaction rate increases when the concentration of H<sub>2</sub>O<sub>2</sub> is 1.0 mmol/L, degradation efficiency can reach 99%, and the concentration of H<sub>2</sub>O<sub>2</sub> is 2.0 mmol/L, degradation effect not ascend, only improve reaction rate, therefore, The H<sub>2</sub>O<sub>2</sub> concentration of 1.0 mmol/L is more suitable in line with resource conservation. As the H<sub>2</sub>O<sub>2</sub> concentration was set to 1.0 mmol/L, the effects of pH on degradation TC were also studied (Fig. S9). When the pH value of the solution increases from 2 to 3 and 4, the degradation efficiency of TC is improved. It might be due to that the reactive oxygen species would be scavenged by H<sup>+</sup> under the acidic pH [50,51], and the corrosion rate of the catalyst also increases. When the pH increased from 4 to 8, the degradation efficiency of TC decreased from 98.3% to 82%.

When pH > 4, the degradation rate decreases continuously with the increase of pH values. Herein, the increase of pH might reduce the redox potential of reactive oxygen species and improve the spontaneous decomposition of H<sub>2</sub>O<sub>2</sub> [52,53]. Therefore, FGD-3 has the highest degradation efficiency for TC at pH 4.

The influence of the initial concentration of the TC on the catalytic reaction was also investigated (shown in Fig. 5d), showing that the initial concentration of 10 mg/L and 20 mg/L, and the degradation efficiencies reached 99%. With the increase of TC initial concentration, the degradation efficiency declined slightly, and the reaction rate decreased.

### 3.3. Possible pathway of TC degradation

As shown in Fig. 10, about 70.2% of TOC in TC solution was degraded after 100 min of catalytic reaction, indicating that TC can be mineralized into harmless products in the photo-Fenton catalytic system. These TC degradation intermediates were determined and analyzed by HPLC-MS. Eleven possible intermediates are listed in Table S2, including *m/z* = 472, 445, 417, 405, 399, 374, 342, 306, 287, 274 and 156. Based on the molecular structure of the product and previous studies on TC degradation, four possible decomposition pathways are suggested in Fig. 6.

In the process of the whole light degradation Fenton, these intermediates were produced mainly for two reasons: the loss of the functional groups and ring-opening reaction. For pathway I, the

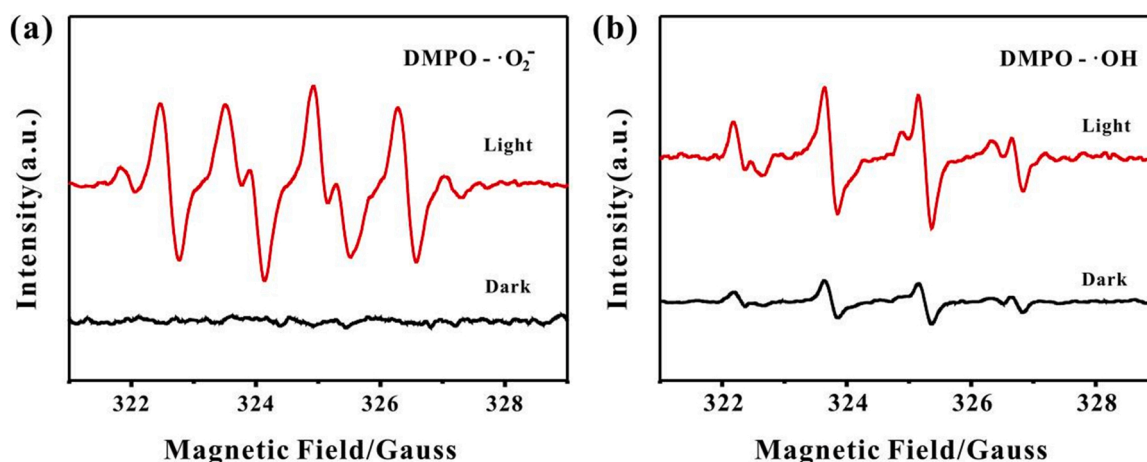


Fig. 8. ESR spectra of ·O<sub>2</sub><sup>-</sup> (a) and ·OH (b) generated by FGD-3 in the presence and absence of visible light irradiation.

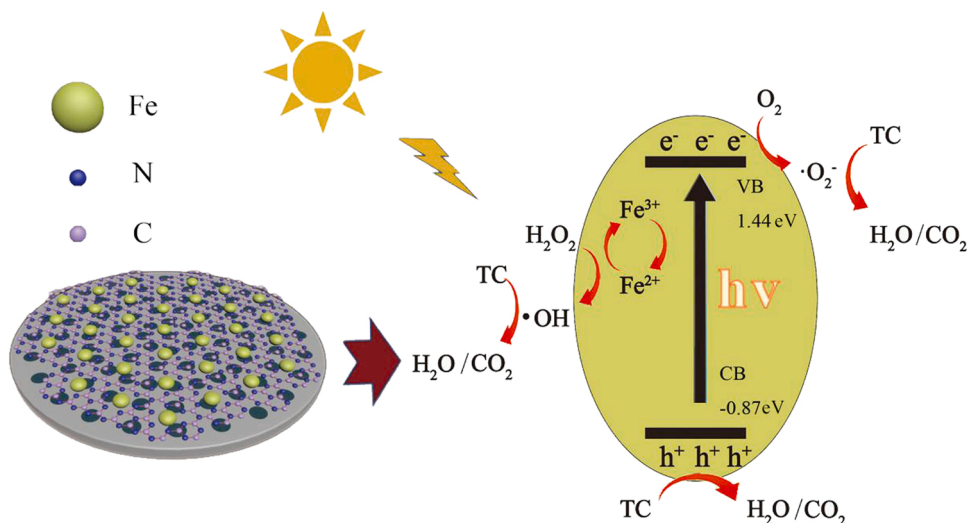


Fig. 9. Possible photo-Fenton degradation mechanism.

generation of TC1 ( $m/z = 472$ ) is attributed to C=C bond cleavage, the rearrangement of  $\cdot\text{OH}$ , and N-methyl oxidation [54]. For Route II, TC2 ( $m/z = 417$ ) is formed by the demethylation of dimethylamino groups. Then,  $\cdot\text{OH}$  continues to attack TC2, TC2 is deamidated to form TC3 ( $m/z = 374$ ), and further dehydration, deamination and hydroxyl form TC4 ( $m/z = 274$ ) and TC6 ( $m/z = 306$ ) [55]. In route III, TC is degraded to TC5 ( $m/z = 405$ ), which is caused by the loss of acyl groups. The rupture of the carbon atom ring of TC5 leads to the formation of TC6 ( $m/z = 306$ ) [56]. In route IV, TC is degraded to TC7 ( $m/z = 399$ ), which is caused by the demethylation of the dimethylamino group and the loss of  $\cdot\text{OH}$ . TC7 is further degraded to TC8 ( $m/z = 342$ ). This is due to the loss of acyl and  $\cdot\text{OH}$  of TC7. TC8 is further degraded to TC9 ( $m/z = 287$ ) [57], and finally degraded to TC10 ( $m/z = 156$ ). The results show that TC can be oxidized into small molecular acids and non-toxic  $\text{CO}_2$  and  $\text{H}_2\text{O}$  in the photo-Fenton catalytic system.

### 3.4. Photo-Fenton degradation mechanism of TC

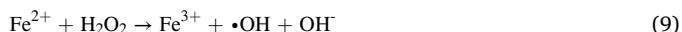
To further study the mechanism of photo-Fenton catalysis, the experiment of activated free radical capture was carried out. In the photodegradation process, hydroxyl radical ( $\cdot\text{OH}$ ), superoxide radical ( $\cdot\text{O}_2^-$ ), and hole ( $\text{h}^+$ ) are generally considered as the main reactive species. To test the effects of these active substances, disodium ethylenediaminetetraacetic acid salt (EDTA-2Na), tert-butanol (TBA), and p-benzoquinone (BQ) were used as scavenging agents for  $\text{h}^+$ ,  $\cdot\text{OH}$  and  $\cdot\text{O}_2^-$ , respectively [58,59]. As can be seen from Fig. 7a, the degradation efficiency of TC was significantly inhibited after the addition of TBA, BQ, and EDTA-2Na, indicating that  $\cdot\text{OH}$ ,  $\cdot\text{O}_2^-$  and  $\text{h}^+$  all played a role in the catalytic process. The degradation efficiency decreased with the addition of TBA, which indicated that  $\cdot\text{OH}$  had little effect on the degradation of TC, and the degradation efficiency of TC was inhibited most obviously with the addition of EDTA-2Na. The minimum reaction rate constant  $k_4$  is also confirmed in Fig. 7b. Therefore, in the FGD-3/ $\text{H}_2\text{O}_2$ /light system, the order of the effect of active free radicals on TC degradation is  $\text{h}^+ > \cdot\text{O}_2^- > \cdot\text{OH}$ .

The active substances in the optical Fenton system were further analyzed by ESR spectroscopy, and the corresponding results are shown in Fig. 8. In Fig. 8a, the  $\cdot\text{O}_2^-$  signal was not observed under dark conditions, but an obvious DMPO- $\cdot\text{O}_2^-$  signal was observed under the irradiation of the 300 W xenon lamp. The results show that  $\cdot\text{O}_2^-$  is a major active species and plays an important role in photocatalytic degradation.  $\cdot\text{OH}$  in the reaction was also studied. As can be seen in Fig. 8b, a weak  $\cdot\text{OH}$  signal can be observed under dark conditions, and the signal of DMPO- $\cdot\text{OH}$  is enhanced under the irradiation of a 300 W xenon lamp.

$\cdot\text{OH}$  and  $\cdot\text{O}_2^-$  exist in the reaction system, which is consistent with the results of free radical trapping experiments.

According to the experimental results, we proposed the possible enhancement mechanism of photo-Fenton catalytic activity of the FGD-3 catalyst as shown in Fig. 9. The FGD-3 catalyst produces photogenerated electrons and holes after being excited by visible light. Because the reduction potential of  $\text{Fe}^{3+}/\text{Fe}^{2+}$  (+0.771 eV vs NHE) is located between the valence band (VB) and conduction band (CB) of g- $\text{C}_3\text{N}_4$ ,  $\text{Fe}^{3+}$  can capture photogenerated electrons to produce  $\text{Fe}^{2+}$ , and the captured electrons react with the electron acceptor (e.g.  $\text{O}_2$ ) to form superoxide radicals ( $\cdot\text{O}_2^-$ ). However, the potential of the valence band is lower than the potential of  $\cdot\text{OH}/\text{OH}^-$  and  $\cdot\text{OH}/\text{H}_2\text{O}$ , and  $\cdot\text{OH}$  cannot be generated [60].  $\text{Fe}^{3+}$  reacts with  $\text{e}^-/\text{H}_2\text{O}_2$  to form  $\text{Fe}^{2+}$ , and the resulting  $\text{Fe}^{2+}$  continues to react with  $\text{H}_2\text{O}_2$  to form  $\text{Fe}^{3+}$ , the rapid cycle between  $\text{Fe}^{3+}$  and  $\text{Fe}^{2+}$  not only accelerates the electron migration rate but also inhibits the recombination of photo-generated electrons and holes. Simultaneously, the reaction also produces oxidative  $\cdot\text{OH}$  radicals [40], in the reaction  $\text{H}_2\text{O}_2$  promotes the cycle between  $\text{Fe}^{3+}/\text{Fe}^{2+}$ . Due to the rapid consumption of  $\text{e}^-$ , a large number of highly oxidizing  $\text{h}^+$  and  $\cdot\text{O}_2^-$  radicals are generated, which can directly degrade organic pollutants.  $\cdot\text{OH}$  radicals produced in the reaction process also have a degradation effect on TC. In conclusion, Fe doping into the lattice of g- $\text{C}_3\text{N}_4$  changes the electronic structure of g- $\text{C}_3\text{N}_4$  and forms a new impurity band for g- $\text{C}_3\text{N}_4$ , which promotes the separation of photogenerated electrons and holes and reduces the resistance of charge transfer. In addition, Fe doping leads to the decrease of bandgap and the increase of visible light absorption. All these factors contribute to the enhancement of photocatalytic activity.

Part of the reaction process can be described as follows (Eqs. (2)–(10)):



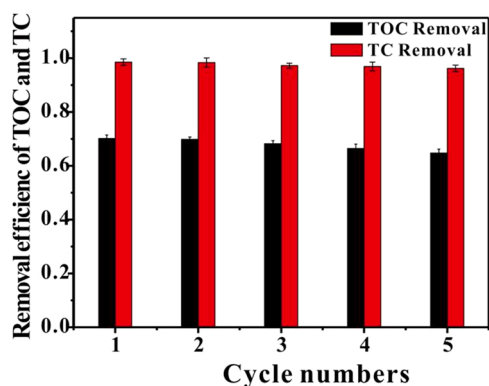
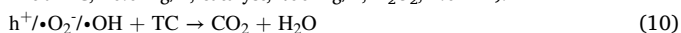


Fig. 10. Removal efficiency of TOC and TC. (Reaction conditions: pH 4.0; initial TC, 20.0 mg/L; catalyst, 400 mg/L;  $\text{H}_2\text{O}_2$ , 1.0 mM).



### 3.5. Stability and reusability of catalyst

The reusability and stability of the catalyst are important indicators in practical applications and the important significance of the catalyst preparation. The stability and reproducibility of the catalyst have been studied through repeated experiments. The dosage of the FGD-3 sample was set at 0.4 g/L, and the initial concentration of TC was 20 mg/L. After the experiment, the catalyst sample was collected and washed with deionized water 3 times with a neutral pH. The solution was centrifuged and then dried at 80 °C. As shown in Fig. 10, after 5 repeated tests, the TC removal rate using FGD-3 remained 96%. The TOC mineralization effect of FGD-3 catalyst 5 times and the amount of iron leaching were also studied. In Fig. 10, the TOC degradation rate of TC was still 64.8% after five cycles. In the catalytic system, the total iron concentration is 1.5 mg/L. As shown in Fig. S10, after each cycle, the amount of leaching iron in the whole solution gradually decreased from 0.067 mg/L to 0.065 mg/L, and the leaching rate of iron decreased relatively low. From Fig. S3, the XPS diagram of the catalyst after five cycles showed that  $\text{Fe}^{3+}$  increased and  $\text{Fe}^{2+}$  decreased in the spectrum of Fe2p, which also proved the conversion between  $\text{Fe}^{3+}$  and  $\text{Fe}^{2+}$  reactions. These results indicate that the FGD-3 catalyst has excellent reusability and stability, and has a broad application prospect in the treatment of organic pollutants.

## 4. Conclusions

A new type of diatomite-supported iron-doped carbon nitride catalyst was synthesized by simple thermal polymerization. The appropriate doping amount of Fe makes the catalyst have higher visible light absorption and higher TC degradation performance. The results showed that the low concentration of  $\text{H}_2\text{O}_2$  (1 mmol/L) and a wide pH value (2–7) showed excellent catalytic activity for TC. The  $\text{h}^+$  produced by FGD-3 in the catalytic process plays a major role in the removal of TC. It is found that the catalyst has good stability and reusability after five repeated experiments. These results indicate that the FGD-3 photo-Fenton catalyst has great potential in the removal of organic pollutants.

### CRedit authorship contribution statement

**Yu Zhang:** Methodology, Validation, Writing – original draft, Funding acquisition. **Xing Chen:** Validation, Investigation, Writing – review & editing. **Min-Shu Cui:** Methodology, Validation, Writing – original draft. **Zhi Guo:** Writing – review & editing. **Yi-Han Chen:** Methodology, Validation. **Kang-Ping Cui:** Methodology, Validation. **Zhao-Gang Ding:** Writing – review & editing. **Rohan Weerasooriya:**

Conceptualization, Writing – review & editing.

### Declaration of Competing Interest

The authors declare that they have no known competing financial interests or personal relationships that could have appeared to influence the work reported in this paper.

### Acknowledgements

The authors acknowledge the financial support from the National Key R&D Program of China (2019YFC0408500), and Key Science and Technology Projects of Anhui Province (202003a07020004). R. W. acknowledges the Program of Distinguished Professor in B&R Countries (Grant No. G20200012010).

### Appendix A. Supporting information

Supplementary data associated with this article can be found in the online version at doi:10.1016/j.jece.2022.107406.

### References

- [1] T. Yang, T. Ma, L. Yang, W. Dai, S. Zhang, S. Luo, A self-supporting UiO-66 photocatalyst with Pd nanoparticles for efficient degradation of tetracycline, *Appl. Surf. Sci.* 544 (2021), 148928.
- [2] N.A. Al-Dhabi, G.A. Esmail, M. Valan Arasu, Effective degradation of tetracycline by manganese peroxidase producing *Bacillus velezensis* strain Al-Dhabi 140 from Saudi Arabia using fibrous-bed reactor, *Chemosphere* 268 (2021), 128726.
- [3] Y. Shi, H. Lin, J. Ma, R. Zhu, W. Sun, X. Lin, J. Zhang, H. Zheng, X. Zhang, Degradation of tetracycline antibiotics by *Arthrobacter nicotianae* OTC-16, *J. Hazard. Mater.* 403 (2021), 123996.
- [4] G. Sharma, S. Bhogal, A. Kumar, M. Naushad, S. Sharma, T. Ahamad, F.J. Stadler, AgO/MgO/FeO/Si<sub>3</sub>N<sub>4</sub> nanocomposite with robust adsorption capacity for tetracycline antibiotic removal from aqueous system, *Adv. Powder Technol.* 31 (2020) 4310–4318.
- [5] H. Chen, M. Huang, Z. Wang, P. Gao, T. Cai, J. Song, Y. Zhang, L. Meng, Enhancing rejection performance of tetracycline resistance genes by a TiO<sub>2</sub>/AgNPs-modified nanofiber forward osmosis membrane, *Chem. Eng. J.* 382 (2020), 123052.
- [6] W. Gu, X. Huang, Y. Tian, M. Cao, L. Zhou, Y. Zhou, J. Lu, J. Lei, Y. Zhou, L. Wang, Y. Liu, J. Zhang, High-efficiency adsorption of tetracycline by cooperation of carbon and iron in a magnetic Fe/porous carbon hybrid with effective Fenton regeneration, *Appl. Surf. Sci.* 538 (2021), 147813.
- [7] C. Song, H.-Y. Liu, S. Guo, S.-G. Wang, Photolysis mechanisms of tetracycline under UV irradiation in simulated aquatic environment surrounding limestone, *Chemosphere* 244 (2020), 125582.
- [8] Z. Lin, Z. Zhen, S. Luo, L. Ren, Y. Chen, W. Wu, W. Zhang, Y.-Q. Liang, Z. Song, Y. Li, D. Zhang, Effects of two ecological earthworm species on tetracycline degradation performance, pathway and bacterial community structure in laterite soil, *J. Hazard. Mater.* 412 (2021), 125212.
- [9] V. Emzhina, E. Kuzin, E. Babusenko, N. Krutchinina, Photodegradation of tetracycline in presence of H<sub>2</sub>O<sub>2</sub> and metal oxide based catalysts, *J. Water Process Eng.* 39 (2021), 101696.
- [10] B. Palanivel, M. Shkir, T. Alshahrani, A. Mani, Novel NiFe<sub>2</sub>O<sub>4</sub> deposited S-doped g-C<sub>3</sub>N<sub>4</sub> nanorod: Visible-light-driven heterojunction for photo-Fenton like tetracycline degradation, *Diam. Relat. Mater.* 112 (2021), 108148.
- [11] S. Xin, B. Ma, G. Liu, X. Ma, C. Zhang, X. Ma, M. Gao, Y. Xin, Enhanced heterogeneous photo-Fenton-like degradation of tetracycline over CuFeO<sub>2</sub>/biochar catalyst through accelerating electron transfer under visible light, *J. Environ. Manag.* 285 (2021), 112093.
- [12] D.A. Tran, C.T. Nguyen Pham, T. Nguyen Ngoc, H. Nguyen Phi, Q.T. Hoai, Ta Truong D.H., V.T. Nguyen, H.H. Luc, L.T. Nguyen, N.N. Dao, S.J. Kim, V. Vo, One-step synthesis of oxygen doped g-C<sub>3</sub>N<sub>4</sub> for enhanced visible-light photodegradation of Rhodamine B, *J. Phys. Chem. Solids* 151 (2021), 109900.
- [13] Y. Li, X. Xing, J. Pei, R. Li, Y. Wen, S. Cui, T. Liu, Automobile exhaust gas purification material based on physical adsorption of tourmaline powder and visible light catalytic decomposition of g-C<sub>3</sub>N<sub>4</sub>/BiVO<sub>4</sub>, *Ceram. Int.* 46 (2020) 12637–12647.
- [14] B. Guo, Y. Tang, Z. Liu, Z. Zhu, G. Yan, Numerical study on optoelectronic properties of alkaline-earth metal doped g-C<sub>3</sub>N<sub>4</sub>, *Chem. Phys.* 544 (2021), 111104.
- [15] W. Zhang, J. Wang, Z. Liu, Y. Pi, R. Tan, Visible light-driven oxidant-free dehydrogenation of alcohols in water using porous ultrathin g-C<sub>3</sub>N<sub>4</sub> nanosheets, *Green Energy Environ.* (2020).
- [16] S. Ji, Y. Yang, Z. Zhou, X. Li, Y. Liu, Photocatalysis-Fenton of Fe-doped g-C<sub>3</sub>N<sub>4</sub> catalyst and its excellent degradation performance towards RhB, *J. Water Process Eng.* (2020), 101804.
- [17] Y. Chen, F. Su, H. Xie, R. Wang, C. Ding, J. Huang, Y. Xu, L. Ye, One-step construction of S-scheme heterojunctions of N-doped MoS<sub>2</sub> and S-doped g-C<sub>3</sub>N<sub>4</sub> for enhanced photocatalytic hydrogen evolution, *Chem. Eng. J.* 404 (2021), 126498.

- [18] M. Faisal, M. Jalalah, F.A. Harraz, A.M. El-Toni, A. Khan, M.S. Al-Assiri, Au nanoparticles-doped g-C<sub>3</sub>N<sub>4</sub> nanocomposites for enhanced photocatalytic performance under visible light illumination, *Ceram. Int.* 46 (2020) 22090–22101.
- [19] M.B. Shekardasht, M.H. Givianrad, P. Gharbani, Z. Mirjafary, A. Mehrizad, Preparation of a novel Z-scheme g-C<sub>3</sub>N<sub>4</sub>/RGO/Bi<sub>2</sub>Fe<sub>4</sub>O<sub>9</sub> nanophotocatalyst for degradation of Congo Red dye under visible light, *Diam. Relat. Mater.* 109 (2020), 108008.
- [20] X. Wang, M. He, Z. Nan, Effects of adsorption capacity and activity site on Fenton-like catalytic performance for Na and Fe co-doped g-C<sub>3</sub>N<sub>4</sub>, *Sep. Purif. Technol.* 256 (2021), 117765.
- [21] W. Zhang, Z. Bian, X. Xin, L. Wang, X. Geng, H. Wang, Comparison of visible light driven H<sub>2</sub>O<sub>2</sub> and peroxymonosulfate degradation of norfloxacin using Co/g-C<sub>3</sub>N<sub>4</sub>, *Chemosphere* 262 (2021), 127955.
- [22] X. Wang, Z. Nan, Highly efficient Fenton-like catalyst Fe-g-C<sub>3</sub>N<sub>4</sub> porous nanosheets formation and catalytic mechanism, *Sep. Purif. Technol.* 233 (2020), 116023.
- [23] Z. Sun, C. Li, G. Yao, S. Zheng, In situ generated g-C<sub>3</sub>N<sub>4</sub>/TiO<sub>2</sub> hybrid over diatomite supports for enhanced photodegradation of dye pollutants, *Mater. Des.* 94 (2016) 403–409.
- [24] H. He, J. Li, C. Yu, Z. Luo, Surface decoration of microdisk-like g-C<sub>3</sub>N<sub>4</sub>/diatomite with Ag/AgCl nanoparticles for application in Cr(VI) reduction, *Sustain. Mater. Technol.* 22 (2019), e00127.
- [25] Q. Sun, X. Hu, S. Zheng, J. Zhang, J. Sheng, Effect of calcination on structure and photocatalytic property of N-TiO<sub>2</sub>/g-C<sub>3</sub>N<sub>4</sub>/diatomite hybrid photocatalyst for improving reduction of Cr(VI), *Environ. Pollut.* 245 (2019) 53–62.
- [26] C. Xiong, Q. Ren, X. Liu, Z. Jin, Y. Ding, H. Zhu, J. Li, R. Chen, Fenton activity on RhB degradation of magnetic g-C<sub>3</sub>N<sub>4</sub>/diatomite/Fe<sub>3</sub>O<sub>4</sub> composites, *Appl. Surf. Sci.* 543 (2021), 148844.
- [27] F. Yuan, Z. Sun, C. Li, Y. Tan, X. Zhang, S. Zheng, Multi-component design and in-situ synthesis of visible-light-driven SnO<sub>2</sub>/g-C<sub>3</sub>N<sub>4</sub>/diatomite composite for high-efficient photoreduction of Cr(VI) with the aid of citric acid, *J. Hazard. Mater.* 396 (2020), 122694.
- [28] X.H. Wang, Z.D. Nan, Highly efficient Fenton-like catalyst Fe-g-C<sub>3</sub>N<sub>4</sub> porous nanosheets formation and catalytic mechanism, *Sep Purif. Technol.* 233 (2020), 116023.
- [29] S. Wu, C. Wang, Y. Jin, G. Zhou, L. Zhang, P. Yu, L. Sun, Green synthesis of reusable super-paramagnetic diatomite for aqueous nickel (II) removal, *J. Colloid Interface Sci.* 582 (2021) 1179–1190.
- [30] Y. Liu, J. Zhang, X. Sheng, N. Li, Q. Ping, Adsorption and release kinetics, equilibrium, and thermodynamic studies of hymexazol onto diatomite, *ACS Omega* 5 (2020) 29504–29512.
- [31] V. Pham Van, C. Duong Van, H. Nguyen Quoc, D. Nguyen Ngoc, T. Cao Minh, Visible-light-induced photo-Fenton degradation of rhodamine B over Fe<sub>2</sub>O<sub>3</sub>-diatomite materials, *J. Sci. Adv. Mater. Devices* 5 (2020) 308–315.
- [32] X. Liu, S. Ye, Y. Qiao, G. Dong, Q. Zhang, J. Qiu, Facile synthetic strategy for efficient and multi-color fluorescent BCNO nanocrystals, *Chem. Commun.* (2009) 4073–4075.
- [33] Q. Zhong, H. Lan, M. Zhang, H. Zhu, M. Bu, Preparation of heterostructure g-C<sub>3</sub>N<sub>4</sub>/ZnO nanorods for high photocatalytic activity on different pollutants (MB, RhB, Cr(VI) and eosin, *Ceram. Int.* 46 (2020) 12192–12199.
- [34] W. Lei, D. Portehault, R. Dimova, M. Antonietti, Boron carbon nitride nanostructures from salt melts: tunable water-soluble phosphors, *J. Am. Chem. Soc.* 133 (2011) 7121–7127.
- [35] T. Doan, An Chi Thanh Nguyen P., N. Tri Nguyen, P. Hung Nguyen, T. Qui Thanh Hoai, T. Duy Huong, N. Van Thang, L. Huy Hoang, N. Le Tuan, D. Ngoc Nhiem, S. J. Kim, V. Vien, One-step synthesis of oxygen doped g-C<sub>3</sub>N<sub>4</sub> for enhanced visible-light photodegradation of Rhodamine B, *J. Phys. Chem. Solids* 151 (2021).
- [36] X. Zhu, Y. Wang, Y. Guo, J. Wan, Y. Yan, Y. Zhou, C. Sun, Environment-friendly synthesis of heterojunction photocatalysts g-C<sub>3</sub>N<sub>4</sub>/BiPO<sub>4</sub> with enhanced photocatalytic performance, *Appl. Surf. Sci.* 544 (2021), 148872.
- [37] Z. Zhao, W. Zhang, W. Liu, Y. Li, J. Ye, J. Liang, M. Tong, Activation of sulfite by single-atom Fe deposited graphitic carbon nitride for diclofenac removal: the synergistic effect of transition metal and photocatalysis, *Chem. Eng. J.* 407 (2021), 127167.
- [38] H. Li, C. Shan, B. Pan, Development of Fe-doped g-C<sub>3</sub>N<sub>4</sub>/graphite mediated peroxymonosulfate activation for degradation of aromatic pollutants via nonradical pathway, *Sci. Total Environ.* 675 (2019) 62–72.
- [39] X. Chi, F. Liu, Y. Gao, J. Song, R. Guan, H. Yuan, An efficient B/Na co-doped porous g-C<sub>3</sub>N<sub>4</sub> nanosheets photocatalyst with enhanced photocatalytic hydrogen evolution and degradation of tetracycline under visible light, *Appl. Surf. Sci.* 576 (2022), 151837.
- [40] J. Hu, P. Zhang, W. An, L. Liu, Y. Liang, W. Cui, In-situ Fe-doped g-C<sub>3</sub>N<sub>4</sub> heterogeneous catalyst via photocatalysis-Fenton reaction with enriched photocatalytic performance for removal of complex wastewater, *Appl. Catal. B Environ.* 245 (2019) 130–142.
- [41] G. Bhargava, I. Gouzman, C.M. Chun, T.A. Ramanarayanan, S.L. Bernasek, Characterization of the “native” surface thin film on pure polycrystalline iron: a high resolution XPS and TEM study, *Appl. Surf. Sci.* 253 (2007) 4322–4329.
- [42] J. Xiao, Q. Han, Y. Xie, J. Yang, Q. Su, Y. Chen, H. Cao, Is C<sub>3</sub>N<sub>4</sub> chemically stable toward reactive oxygen species in sunlight-driven water treatment? *Environ. Sci. Technol.* 51 (2017) 13380–13387.
- [43] C. Ding, S. Kang, W. Li, W. Gao, Z. Zhang, L. Zheng, L. Cui, Mesoporous structure and amorphous Fe-N sites regulation in Fe-g-C<sub>3</sub>N<sub>4</sub> for boosted visible-light-driven photo-Fenton reaction, *J. Colloid Interface Sci.* 608 (2020) 2515–2528.
- [44] L. Wang, H.-g Zhang, C.-y Guo, L.-j Feng, C.-h Li, W.-t Wang, Facile constructing plasmonic Z-scheme Au NPs/g-C<sub>3</sub>N<sub>4</sub>/BiOBr for enhanced visible light photocatalytic activity, *J. Fuel Chem. Technol.* 47 (2019) 834–842.
- [45] P. Wu, C. Zhou, Y. Li, M. Zhang, P. Tao, Q. Liu, W. Cui, Flower-like FeOOH hybridized with carbon quantum dots for efficient photo-Fenton degradation of organic pollutants, *Appl. Surf. Sci.* 540 (2021), 148362.
- [46] M. Wang, C. Jin, J. Kang, J. Liu, Y. Tang, Z. Li, S. Li, CuO/g-C<sub>3</sub>N<sub>4</sub> 2D/2D heterojunction photocatalysts as efficient peroxymonosulfate activators under visible light for oxytetracycline degradation: Characterization, efficiency and mechanism, *Chem. Eng. J.* 13 (2020), 128118.
- [47] L. Liu, Y. Qi, J. Lu, S. Lin, W. An, Y. Liang, W. Cui, A stable Ag<sub>3</sub>PO<sub>4</sub>@g-C<sub>3</sub>N<sub>4</sub> hybrid core@shell composite with enhanced visible light photocatalytic degradation, *Appl. Catal. B Environ.* 183 (2016) 133–141.
- [48] X.-H. Jiang, Q.-J. Xing, X.-B. Luo, F. Li, J.-P. Zou, S.-S. Liu, X. Li, X.-K. Wang, Simultaneous photoreduction of uranium(VI) and photooxidation of arsenic (III) in aqueous solution over g-C<sub>3</sub>N<sub>4</sub>/TiO<sub>2</sub> heterostructured catalysts under simulated sunlight irradiation, *Appl. Catal. B Environ.* 228 (2018) 29–38.
- [49] T. Giannakopoulou, I. Papailias, N. Todorova, N. Boukos, Y. Liu, J. Yu, C. Trapalis, Tailoring the energy band gap and edges’ potentials of g-C<sub>3</sub>N<sub>4</sub>/TiO<sub>2</sub> composite photocatalysts for NO<sub>x</sub> removal, *Chem. Eng. J.* 310 (2017) 571–580.
- [50] J. Bai, Y. Liu, X. Yin, H. Duan, J. Ma, Efficient removal of nitrobenzene by Fenton-like process with Co-Fe layered double hydroxide, *Appl. Surf. Sci.* 416 (2017) 45–50.
- [51] X. Liu, Z. Cao, Z. Yuan, J. Zhang, X. Guo, Y. Yang, F. He, Y. Zhao, J. Xu, Insight into the kinetics and mechanism of removal of aqueous chlorinated nitroaromatic antibiotic chloramphenicol by nanoscale zero-valent iron, *Chem. Eng. J.* 334 (2018) 508–518.
- [52] Y. Liu, Q. Fan, J. Wang, Zn-Fe-CNTs catalytic in situ generation of H<sub>2</sub>O<sub>2</sub> for Fenton-like degradation of sulfamethoxazole, *J. Hazard. Mater.* 342 (2018) 166–176.
- [53] J. Tang, J. Wang, Metal organic framework with coordinatively unsaturated sites as efficient fenton-like catalyst for enhanced degradation of sulfamethazine, *Environ. Sci. Technol.* 52 (2018) 5367–5377.
- [54] X.-D. Zhu, Y.-J. Wang, R.-J. Sun, D.-M. Zhou, Photocatalytic degradation of tetracycline in aqueous solution by nanosized TiO<sub>2</sub>, *Chemosphere* 92 (2013) 925–932.
- [55] X. Li, K. Cui, Z. Guo, T. Yang, Y. Cao, Y. Xiang, H. Chen, M. Xi, Heterogeneous Fenton-like degradation of tetracyclines using porous magnetic chitosan microspheres as an efficient catalyst compared with two preparation methods, *Chem. Eng. J.* 379 (2020), 122324.
- [56] W. Wang, K. Xiao, L. Zhu, Y. Yin, Z. Wang, Graphene oxide supported titanium dioxide & ferrous oxide hybrid, a magnetically separable photocatalyst with enhanced photocatalytic activity for tetracycline hydrochloride degradation, *RSC Adv.* 7 (2017) 21287–21297.
- [57] Y.-Y. Chen, Y.-L. Ma, J. Yang, L.-Q. Wang, J.-M. Lv, C.-J. Ren, Aqueous tetracycline degradation by H<sub>2</sub>O<sub>2</sub> alone: removal and transformation pathway, *Chem. Eng. J.* 307 (2017) 15–23.
- [58] J. Jiang, X. Wang, Y. Liu, Y. Ma, T. Li, Y. Lin, T. Xie, S. Dong, Photo-Fenton degradation of emerging pollutants over Fe-POM nanoparticle/porous and ultrathin g-C<sub>3</sub>N<sub>4</sub> nanosheet with rich nitrogen defect: degradation mechanism, pathways, and products toxicity assessment, *Appl. Catal. B Environ.* 278 (2020), 119349.
- [59] S.-W. Lv, J.-M. Liu, N. Zhao, C.-Y. Li, F.-E. Yang, Z.-H. Wang, S. Wang, MOF-derived CoFe<sub>2</sub>O<sub>4</sub>/Fe<sub>2</sub>O<sub>3</sub> embedded in g-C<sub>3</sub>N<sub>4</sub> as high-efficient Z-scheme photocatalysts for enhanced degradation of emerging organic pollutants in the presence of persulfate, *Sep. Purif. Technol.* 253 (2020), 117413.
- [60] H. Zhang, L. Jia, P. Wu, R. Xu, J. He, W. Jiang, Improved H<sub>2</sub>O<sub>2</sub> photogeneration by KOH-doped g-C<sub>3</sub>N<sub>4</sub> under visible light irradiation due to synergistic effect of N defects and K modification, *Appl. Surf. Sci.* 527 (2020), 146584.